

Linearized Inflow and Interference Models from High Fidelity Free Wake Analysis for Modern Rotorcraft Configurations

Jeffrey D. Keller
Senior Associate

Robert M. McKillip, Jr.
Senior Associate
Continuum Dynamics, Inc.
Ewing, NJ, USA

Daniel A. Wachspress
Senior Associate

Mark J. S. Lopez
Aerospace Engineer

Mark B. Tischler
Senior Technologist Flight
Control Technology

Ondrej Juhasz
Assistant Professor

US Army Combat Capabilities Development Command
Aviation & Missile Center
Moffett Field, CA, USA

US Naval Academy
Annapolis, MD, USA

ABSTRACT

Linearized inflow models have been used to represent dynamic wake effects for control law development and flight dynamics simulation of conventional main rotor / tail rotor helicopters. With the current focus in the industry toward high-speed concepts and electric vertical take-off and landing (eVTOL) aircraft, modern rotorcraft designs are trending away from the conventional main rotor / tail rotor configuration for which low-order dynamic inflow models have been applied and validated. Configurations currently in design and flight testing stages include coaxial, coaxial-compound, tiltrotor, multi-rotor, and augmented lift concepts that involve strong rotor-rotor and rotor-airframe aerodynamic interactions. A procedure for extracting linearized inflow and interference models from higher fidelity comprehensive analyses suitable for advanced rotorcraft configurations has been developed and applied to a modern lift-offset coaxial rotorcraft. A second-order inflow model structure including wake distortion effects due to pitch and roll motion is shown to capture the critical dynamic response characteristics when compared to a nonlinear flight dynamics simulation coupled with a free wake model. This second-order model structure is more accurate and provides better prediction of flight controller performance metrics than a more conventional Pitt-Peters model structure.

NOTATION

C_T, C_L, C_M	Aerodynamic thrust, roll moment, and pitch moment coefficients	K_N	Second-order inflow near wake gain matrix
$G_{oL}^U, G_{sL}^U, G_{cL}^U$	Lower-to-upper rotor inflow interference gains	K_{Req}	Equivalent inflow wake distortion coefficient
$G_{oU}^L, G_{sU}^L, G_{cU}^L$	Upper-to-lower rotor inflow interference gains	L, M	Inflow static gain and apparent mass matrices
K_1, K_2, K_3	Second-order inflow model wake distortion coefficients	p_T, q_T	Rotor tip path plane roll and pitch rate
K_F	Second-order inflow far wake gain matrix	Θ_T	Rotor tip path plane pitch displacement
K_M	Second-order inflow near/far wake coupling coefficient (matrix)	η	Lagged inflow state
		λ	Rotor inflow
		$\lambda_o, \lambda_s, \lambda_c$	Uniform and harmonic inflow states
		λ_f	Inflow state associated with far wake effects
		τ_d	Coaxial upper-to-lower rotor delay time (sec)
		τ_f	Time constant associated with far-field wake distortion effects (sec)
		τ_i	Inflow time constant (sec)
		$()_s, ()_c$	State / parameter associated with sine and cosine inflow harmonics
		$()^L, ()^U$	State / parameter associated with lower and upper rotor of coaxial rotor system

Presented at the Vertical Flight Society's 76th Annual Forum & Technology Display, Virginia Beach, Virginia, USA, Oct. 6-8, 2020. Copyright © 2020 by the Vertical Flight Society. All rights reserved. Distribution Statement A: approved for public release; distribution is unlimited.

INTRODUCTION

Rotorcraft flight dynamics modeling and simulation is cross-disciplinary and requires accurate models of the rotor system aerodynamics and dynamics, in addition to interactional effects with the airframe. Modern rotorcraft configurations including electric vertical take-off and landing (eVTOL) aircraft increasingly are based on multi-rotor and coaxial rotor systems. These configurations tend to have more significant rotor-to-rotor and rotor-to-airframe interactions than conventional single main rotor helicopters. Modeling of these advanced rotorcraft configurations is not accurately represented by conventional dynamic inflow models (Refs. 1, 2) as demonstrated by Juhasz et al. (Ref. 3). Higher fidelity methods such as comprehensive free vortex analyses and/or computational fluid dynamics (CFD) are required. These high-order methods can be used for engineering analysis but are not well suited for flight control development or real-time piloted simulation, which are the primary applications of rotorcraft flight dynamics model development.

Recent work (Refs. 4-10) has focused on using parameter identification methods to extract linearized inflow models from comprehensive free wake and CFD analyses. The primary motivation for this work has been to derive inflow models that retain the characteristics of dynamic inflow / finite-state inflow models (Refs. 1, 2) commonly used in rotorcraft flight simulation applications. Unlike conventional dynamic inflow models, the current model structure is formulated to capture more complex aerodynamic phenomena that can occur in modern rotorcraft configurations. Recent work (Refs. 8, 9) has also shown that the inflow dynamics, including wake distortion due to maneuvering flight and rotor wake interference effects, require a higher-order model structure. This model structure retains a three-state inflow expansion, in contrast to a multi-state expansion as used for the generalized finite-state inflow model (Ref. 2), and also represents the influence of the far wake distortion at the rotor with additional dynamic states. This model structure was applied to a conventional single main rotor helicopter and coaxial rotorcraft in Ref. 9. This paper expands upon these initial results for a generic coaxial rotorcraft configuration and examines the influence of the inflow model on flight control development.

This paper is outlined as follows. First a brief overview of the inflow model extraction procedure is given, followed by a description of the generic coaxial rotorcraft configuration examined in this paper. The inflow model structure is given next, followed by model identification results. The linearized inflow model is compared with nonlinear simulation results to verify the model. The linearized model is then used to develop a roll-axis controller for hover. Results are presented for both hover and forward flight conditions.

METHODOLOGY OVERVIEW

A brief overview of the methodology for extracting linearized inflow models is provided in this section. Additional details can be found in Refs. 8 and 9. The procedure begins with formulation of a nonlinear simulation model of the target rotorcraft within a generic component-based flight dynamics modeling framework. This model should represent the primary lifting components including rotors and fixed lifting surfaces as conventional blade element (strip theory) modeling techniques and include relevant blade dynamics and flexible modes. Rotor inflow and airframe interference effects are represented using the CHARM Wake Panel Module (Ref. 11), which is a free wake and lifting panel model for the rotorcraft induced velocity field. Aerodynamic loads for the rotor blades and fixed lifting surfaces (e.g., wing for a tiltrotor or tilt-wing configuration) are passed from the generic flight dynamics modeling framework to CHARM, which determines the induced velocity field due to all lifting components including interactional effects, in addition to the wake geometry evolution. This coupling approach has been successfully applied to engineering analysis (Ref. 12) and real-time pilot-in-the-loop simulations (Refs. 13, 14).

To extract linearized inflow models suitable for flight control development and real-time simulation, the nonlinear simulation is trimmed for a target flight condition, which includes successive trim cycles for the airframe and rotor wake solution. Perturbations about the trim solution are applied to the wake and induced velocity field using frequency sweep excitations. Perturbations are applied to the blade loading (circulation distribution) and hub motion. This step produces inflow and interference input-output source data that are used to identify parameters of a linear inflow model structure. Inputs are expressed as aerodynamic force and moment coefficients (i.e., C_T , C_L , C_M) for each component, in addition to the tip path plane motion (e.g., p_T , q_T). Outputs are components of the induced velocity field expansion. Finally, frequency domain inflow model identification is performed using CIPHER[®] (Ref. 15).

A critical step in linear inflow model identification is selection of a suitable model structure. Previous work has used different model structures loosely based on the Pitt-Peters dynamic inflow model. As shown in Ref. 9, the inflow response is second-order in nature (which can be seen by a 40dB per decade roll-off in the inflow response due to aerodynamic loading and tip path plane excitation). Thus, a hybrid model structure is used that extends Pitt-Peters dynamic inflow with additional states and model parameters that represent wake dynamics associated with tip path plane motion. These additional wake dynamics can be much slower than the time constant associated with dynamic inflow depending on the operating condition.

Additional details of the second-order inflow model structure are provided below following a description of the generic coaxial rotorcraft model, which is the focus of this paper.

GENERIC COAX ROTORCRAFT MODEL

The aircraft configuration analyzed in this paper is a generic coaxial rotorcraft (GCR), illustrated in Figure 1, which is a lift-offset helicopter with pusher propeller to achieve high-speed flight. This configuration is representative of a short-haul, medium-lift advanced rotorcraft concept that has been the focus of next-generation vertical lift aircraft research by the US Army Combat Capabilities Development Command Aviation & Missile Center (Ref. 16). The specific configuration layout was derived from an earlier rotorcraft sizing trade-off study (Ref. 17) and has been modified to more closely match the Sikorsky X2 and Sikorsky-Boeing SB>1 coaxial lift-offset configurations. This rotorcraft configuration has been used in flight dynamics and control studies, in addition to inflow model identification investigations (Refs. 7, 9, 10, 18). Basic GCR configuration data are given in Table 1.

Table 1. Generic Coax Rotorcraft (GCR) Configuration Data.

Gross weight	35,200 lbs
Number of blades per rotor	4
Rotor radius	30.55 ft
Rotor separation	51.3 in
Rotor speed, hover	23.7 rad/sec
Rotor speed, cruise	19.0 rad/sec
Number of prop blades	6
Prop radius	6.6 ft
Prop rotational speed	136 rad/sec



Figure 1. Generic Coaxial Rotorcraft (GCR) Configuration (from Ref. 17).

The GCR rotor system is comprised of two counter-rotating hingeless rotors with stiff out-of-plane and in-plane blade degrees of freedom. Blade dynamic and aerodynamic properties are derived from public domain data for the Sikorsky XH-59A Advancing Blade Concept (ABC) rotorcraft. The blade chord and twist distribution are derived from the trade study given in Ref. 17. In this study, the rotor system is modeled as rigid blades with effective hinge offset and spring restraints to match the first flap and lag modes derived from the HeliUM model of Ref. 16. In hover, the non-dimensional flap and lag frequencies are 1.49 and 1.33, respectively. In forward flight cruise, these frequencies become 1.56 and 1.44 due to the reduced rotor speed. The lower rotor rotation direction is counter-clockwise when viewed from above while the upper rotor rotation direction is clockwise, which is opposite to the XH-59A. Rotor swashplate controls include collective, lateral cyclic, and longitudinal cyclic inputs with substantial phase angle ($\Delta_{SP} = 70$ deg) between the swashplate and blade pitch inputs.

The GCR empennage is an “H-tail” configuration with three vertical fins at the center and tips of the horizontal stabilizer. The left and right vertical fins extend above and below the horizontal stabilizer, while the center fin is located below this surface. The center fin area is half of the left/right tip fin area. The horizontal stabilizer includes a full-span elevator, and the left and right vertical fins include full-span rudders. Aerodynamic data for these empennage surfaces are based on open-source data for the XV-15, which is derived from wind-tunnel data.

The pusher propeller is approximated as a rotor disk that generates aerodynamic forces and moments based on a “Bailey-type” model with no additional flapping dynamics. This approach is similar to previous modeling studies for the GCR configuration, as well as flight dynamics models for the X2 configuration (Ref. 19). The pusher prop controls include both collective and lateral cyclic inputs.

Rotor controls are combined into symmetric and differential collective and cyclic inputs. In total, there are 11 independent control inputs for the GCR configuration (6 rotor inputs, 2 pusher prop inputs, 3 empennage control surface inputs), resulting in an over-controlled aircraft. For trim, only the primary rotor controls (symmetric/differential collective, symmetric cyclic) and pusher prop collective are used. Dynamic response characteristics have been examined due to the primary (trim) controls, as well as the secondary control surface deflections and pusher prop inputs.

An illustration of the GCR modeled configuration is illustrated in Figure 2. Note that the fuselage is represented by a generic surface geometry in this illustration and modeled by aerodynamic coefficient data.

COAXIAL ROTOR SYSTEM INFLOW MODEL

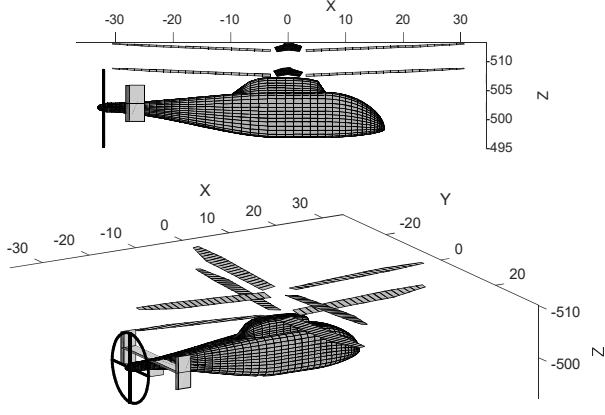


Figure 2. Flight Dynamics Model of GCR Configuration.

Inflow Model Structure

The second-order dynamic inflow model structure for an isolated rotor and coaxial rotor system was given in Ref. 9. This model structure was shown to capture wake distortion effects on the rotor inflow and included additional dynamics associated with the wake dynamics. For a coaxial rotor system, the model structure also captures the rotor-to-rotor interaction that occurs due to the close proximity of the rotors. The model structure is given as follows.

The coaxial rotor inflow model is formulated as three-state dynamic inflow expansions $\lambda^{U,L} = \lambda_o^{U,L} + \lambda_c^{U,L} x \cos \psi + \lambda_s^{U,L} x \sin \psi$ for each rotor. The inflow dynamics for each rotor are determined from the aerodynamic loading and far wake distortion, which are coupled due to superimposition of the combined flow fields. This model structure is the “output-coupled” form in Ref. 8 and is supported by the analytical and numerical study of Ref. 20. Thus, the second-order inflow model structure for coaxial rotor systems is described by the following first-order equations:

$$\begin{aligned}
 L^L M^L \begin{bmatrix} \dot{\tilde{\lambda}}_o^L \\ \dot{\tilde{\lambda}}_s^L \\ \dot{\tilde{\lambda}}_c^L \end{bmatrix} + \begin{bmatrix} \tilde{\lambda}_o^L \\ \tilde{\lambda}_s^L \\ \tilde{\lambda}_c^L \end{bmatrix} &= L^L \begin{bmatrix} C_T \\ C_L \\ C_M \end{bmatrix} + K_N^L \begin{bmatrix} p_T/\Omega \\ q_T/\Omega \\ \Theta_T \end{bmatrix} + \begin{bmatrix} 0 \\ \lambda_{fs} \\ \lambda_{fc} \end{bmatrix} \\
 L^U M^U \begin{bmatrix} \dot{\tilde{\lambda}}_o^U \\ \dot{\tilde{\lambda}}_s^U \\ \dot{\tilde{\lambda}}_c^U \end{bmatrix} + \begin{bmatrix} \tilde{\lambda}_o^U \\ \tilde{\lambda}_s^U \\ \tilde{\lambda}_c^U \end{bmatrix} &= L^U \begin{bmatrix} C_T \\ C_L \\ C_M \end{bmatrix} + K_N^U \begin{bmatrix} p_T/\Omega \\ q_T/\Omega \\ \Theta_T \end{bmatrix} + \begin{bmatrix} 0 \\ -\lambda_{fs} \\ \lambda_{fc} \end{bmatrix} \\
 \begin{bmatrix} \tau_{fs} & 0 \\ 0 & \tau_{fc} \end{bmatrix} \begin{bmatrix} \lambda_{fs} \\ \lambda_{fc} \end{bmatrix} + \begin{bmatrix} \lambda_{fs} \\ \lambda_{fc} \end{bmatrix} &= -K_M^C \begin{bmatrix} \tilde{\lambda}_s^L \\ \tilde{\lambda}_c^L \\ \tilde{\lambda}_s^U \\ \tilde{\lambda}_c^U \end{bmatrix} + K_F \begin{bmatrix} p_T/\Omega \\ q_T/\Omega \end{bmatrix}
 \end{aligned} \tag{1}$$

where p_T , q_T , and Θ_T are the roll rate, pitch rate, and pitch displacement, respectively, of the tip path plane. Terms denoted by (\sim) represent the (local) inflow response of a given rotor (upper or lower) due to its *own* aerodynamic loading and tip path plane motion sources. Forms for the coefficient matrices are provided below. Note that this model structure corresponds to the rotor rotation directions for the GCR configuration; for the opposite rotation convention, the model structure will have similar form but some signs will be reversed.

The total inflow is found from superimposition of the local rotor inflow contributions. For the upper rotor, this relationship can be approximated as follows:

$$\begin{bmatrix} \lambda_o \\ \lambda_s \\ \lambda_c \end{bmatrix}^U = \begin{bmatrix} \tilde{\lambda}_o \\ \tilde{\lambda}_s \\ \tilde{\lambda}_c \end{bmatrix}^U + G_L^U \begin{bmatrix} \tilde{\lambda}_o \\ \tilde{\lambda}_s \\ \tilde{\lambda}_c \end{bmatrix}^L \tag{2}$$

where G_L^U is a diagonal gain matrix accounting for the influence of the lower rotor inflow on the upper rotor inflow.

The relationship for the lower rotor inflow is similar except that a time delay term is included:

$$\begin{bmatrix} \lambda_o \\ \lambda_s \\ \lambda_c \end{bmatrix}^L = \begin{bmatrix} \tilde{\lambda}_o \\ \tilde{\lambda}_s \\ \tilde{\lambda}_c \end{bmatrix}^L + G_{ij}^L \begin{bmatrix} \tilde{\lambda}_o \\ \tilde{\lambda}_s \\ \tilde{\lambda}_c \end{bmatrix}^U e^{-\tau_d s} \quad (3)$$

where G_{ij}^L is a gain matrix accounting for the influence of the upper rotor inflow on the lower rotor inflow. The delay parameter τ_d heuristically represents the time required for a disturbance at the upper rotor to be reach the lower rotor. The time delay is further approximated using a first-order Padé expansion, which leads to additional dynamic states:

$$\begin{bmatrix} \dot{\eta}_o \\ \dot{\eta}_s \\ \dot{\eta}_c \end{bmatrix} = -\frac{2}{\tau_d} \begin{bmatrix} \eta_o \\ \eta_s \\ \eta_c \end{bmatrix} + \frac{4}{\tau_d} \begin{bmatrix} \tilde{\lambda}_o \\ \tilde{\lambda}_s \\ \tilde{\lambda}_c \end{bmatrix}^U \quad (4)$$

and

$$\begin{bmatrix} \lambda_o \\ \lambda_s \\ \lambda_c \end{bmatrix}^L = \begin{bmatrix} \tilde{\lambda}_o \\ \tilde{\lambda}_s \\ \tilde{\lambda}_c \end{bmatrix}^L + G_{ij}^L \left\{ \begin{bmatrix} \eta_o \\ \eta_s \\ \eta_c \end{bmatrix} - \begin{bmatrix} \tilde{\lambda}_o \\ \tilde{\lambda}_s \\ \tilde{\lambda}_c \end{bmatrix}^U \right\} \quad (5)$$

The form of the coefficient matrices for the second-order inflow model are given as follows. The apparent mass and static gain matrices follow from dynamic inflow theory:

$$M^{U,L} = \begin{bmatrix} M_{11}^{U,L} & 0 & 0 \\ 0 & M_{22}^{U,L} & 0 \\ 0 & 0 & M_{33}^{U,L} \end{bmatrix} \quad (6)$$

$$L^{U,L} = \begin{bmatrix} L_{11}^{U,L} & 0 & L_{13}^{U,L} \\ 0 & L_{22}^{U,L} & 0 \\ L_{31}^{U,L} & 0 & L_{33}^{U,L} \end{bmatrix} \quad (7)$$

The form of the wake distortion matrices is given as:

$$K_N^U = \begin{bmatrix} 0 & 0 & 0 \\ -K_{1s} & 0 & 0 \\ 0 & K_{1c} & K_3 \end{bmatrix} \quad (8)$$

$$K_N^L = \begin{bmatrix} 0 & 0 & 0 \\ K_{1s} & 0 & 0 \\ 0 & K_{1c} & K_3 \end{bmatrix} \quad (9)$$

$$K_F = \begin{bmatrix} K_{2s} & 0 \\ 0 & K_{2c} \end{bmatrix} \quad (10)$$

$$K_M^C = \frac{1}{2} \begin{bmatrix} K_{Ms} & 0 & -K_{Ms} & 0 \\ 0 & K_{Mc} & 0 & K_{Mc} \end{bmatrix} \quad (11)$$

Inflow coupling matrices are diagonal matrices defined as follows:

$$G_L^U = \begin{bmatrix} G_{oL}^U & 0 & 0 \\ 0 & G_{sL}^U & 0 \\ 0 & 0 & G_{cL}^U \end{bmatrix} \quad (9)$$

$$G_U^L = \begin{bmatrix} G_{oU}^L & 0 & 0 \\ 0 & G_{sU}^L & 0 \\ 0 & 0 & G_{cU}^L \end{bmatrix} \quad (10)$$

It has been found that constraints should be placed on certain parameters (i.e., $\tau_{fs} = \tau_{fc} \equiv \tau_f$ and $K_{Ms} = K_{Mc} \equiv K_M$) to reduce correlation effects between identified parameters. In summary, the model structure has 11 states, 9 inputs, and 6 outputs with 34 parameters including additional time delays on selected input-output response pairs, as discussed below. In hover and axial flight, additional symmetry constraints can be applied (i.e., $K_{1s} = K_{1c} \equiv K_1$, $K_{2s} = K_{2c} \equiv K_2$) to further reduce the set of free parameters to 17 model parameters.

Inflow Model Identification

Inflow model identification results are presented for the GCR configuration in hover and forward flight trim conditions. In each case, the rotor system was trimmed based on the aircraft gross weight, which corresponded to total thrust coefficient of 0.010 based on the disk area of a single rotor. Inflow response data were generated using CHARM by applying frequency sweep inputs to the upper and lower rotor aerodynamic coefficients, as well as the pitch and roll rate of the rotor system. Inflow frequency response estimation and model parameter identification were performed using CIFER[®] (Ref. 15) based on the model structure described in Eqs. (1) through (10).

Identified inflow model parameters and parameter uncertainty bounds (in parentheses) are summarized in Table 2, and identification costs are summarized in Table 3. As mentioned above, symmetry constraints have been applied to wake distortion and upper-lower coupling parameters in hover. For forward flight conditions, it was found that the inflow model structure was unable to capture the phase lag observed in the cosine inflow component response due to thrust inputs. Time delay parameters are included for these input-output pairs, which are tabulated below the physical model parameters.

Table 2. GCR Inflow Model Identified Parameter Values.

Parameter	Hover	80kts	180kts
M_{11}^U	0.185 (5.0%)	0.0683 (4.3%)	0.0428 (7.5%)
M_{22}^U	-0.0304 (4.0%)	-0.0093 (5.0%)	-0.0036 (15%)
M_{33}^U	-0.0304 [†]	-0.0080 (4.8%)	-0.0049 (11%)
L_{11}^U	1.78 (4.5%)	1.95 (3.4%)	0.895 (3.5%)
L_{22}^U	-9.37 (9.6%)	-24.4 (5.9%)	-11.9 (4.0%)
L_{33}^U	-9.37 [†]	-7.97 (5.9%)	-3.91 (4.3%)
L_{13}^U	0 [†]	3.89 (3.2%)	0.936 (3.6%)
L_{31}^U	0 [†]	3.65 (5.0%)	5.48 (12%)
M_{11}^L	0.121 (4.7%)	0.0650 (4.5%)	0.0546 (5.9%)
M_{22}^L	-0.0232 (4.6%)	-0.0100 (4.5%)	-0.0059 (8.9%)
M_{33}^L	-0.0232 [†]	-0.0077 (5.0%)	-0.0036 (11%)
L_{11}^L	3.45 (4.6%)	2.07 (3.5%)	0.920 (3.5%)
L_{22}^L	-12.9 (12%)	-31.7 (7.0%)	-11.1 (4.0%)
L_{33}^L	-12.9 [†]	-11.4 (6.0%)	-4.97 (4.4%)
L_{13}^L	0 [†]	3.26 (3.4%)	1.39 (3.5%)
L_{31}^L	0 [†]	4.23 (5.5%)	4.78 (11%)
G_{oL}^U	0.951 (5.3%)	0.834 (3.8%)	1.12 (3.8%)
G_{sL}^U	-0.783 (2.8%)	-0.760 (3.5%)	-0.781 (4.1%)
G_{cL}^U	0.783 [†]	0.792 (2.4%)	0.217 (11%)
G_{oU}^L	1.22 (5.3%)	1.02 (3.7%)	1.07 (3.9%)
G_{sU}^L	-1.19 (2.8%)	-0.980 (3.9%)	-0.693 (4.0%)
G_{cU}^L	1.19 [†]	0.983 (2.7%)	0.216 (11%)
τ_d	0.019 (18%)	0.013 (23%)	0.029 (14%)
K_{1s}	0.540 (11%)	-0.122 (6.3%)	-0.034 (4.3%)
K_{1c}	0.540 [†]	0 [†]	0 [†]
K_{2s}	0.371 (13%)	0 [†]	0 [†]
K_{2c}	0.371 [†]	-0.201 (4.3%)	0.049 (16%)
K_3	0 [†]	0.492 (5.5%)	-0.769 (4.7%)
K_M	0.906 (22%)	1.29 (7.8%)	0.5 [†]
τ_f [sec]	0.166 (14%)	0.116 (5.7%)	0.040 (24%)
$\tau_{\lambda_c^U/c_T^U}$ [sec]	0 [†]	0.161 (3.8%)	0 [†]
$\tau_{\lambda_c^L/c_T^U}$ [sec]	0 [†]	0.150 (4.3%)	0.052 (13%)
$\tau_{\lambda_c^U/c_T^L}$ [sec]	0 [†]	0.152 (4.0%)	0.027 (27%)
$\tau_{\lambda_c^L/c_T^L}$ [sec]	0 [†]	0.146 (4.2%)	0 [†]

[†] - Parameter fixed or constrained during identification

Table 3. Identified Coaxial Inflow Model Identification Costs for GCR Configuration.

Response	Hover	80kts	180kts
λ_o^u/C_T^u	62.4	60.4	112.3
λ_s^u/C_L^u	22.1	19.9	17.1
λ_c^u/C_M^u	22.2	39.0	20.4
λ_o^u/C_M^u	n/a	70.9	268.6
λ_c^u/C_T^u	n/a	40.9	n/a
λ_o^l/C_T^l	34.4	64.3	109.4
λ_s^l/C_L^l	37.1	32.9	16.6
λ_c^l/C_M^l	26.3	98.0	n/a
λ_o^l/C_M^l	n/a	17.0	118.8
λ_c^l/C_T^l	n/a	82.0	14.6
λ_o^u/C_T^l	33.1	54.6	99.4
λ_s^u/C_L^l	7.9	29.7	17.5
λ_c^u/C_M^l	7.7	53.7	n/a
λ_o^u/C_M^l	n/a	32.8	57.0
λ_c^u/C_T^l	n/a	61.0	9.0
λ_o^l/C_T^l	88.7	39.0	99.3
λ_s^l/C_L^l	15.0	21.8	51.4
λ_c^l/C_M^l	15.2	29.0	23.3
λ_o^l/C_M^l	n/a	139.7	129.3
λ_c^l/C_T^l	n/a	79.6	n/a
$\lambda_s^u/(p_T/\Omega)$	66.1	n/a	n/a
$\lambda_s^l/(p_T/\Omega)$	85.7	129.7	133.9
$\lambda_c^u/(q_T/\Omega)$	51.5	276.8	n/a
$\lambda_c^l/(q_T/\Omega)$	61.9	72.6	75.2
Ave. cost	39.2	70.2	76.3

Typical identified time delays are approximately 150 msec for the 80-kt condition and decrease for higher flight speeds. Identified values for the 80-kt case are somewhat significant and suggests the model structure does not capture all important physical behavior. Note that this behavior is not unique to coaxial rotor systems and was also observed for single rotor helicopters (Ref. 9).

The Cramer-Rao parameter uncertainty bounds (Table 2), which are reported as a percentage of the corresponding

identified parameter value, are typically well below the recommended guideline ($CR \leq 20\%$, Ref. 15), indicating a reliable model identification. The average cost functions (Table 3) are all less than the guideline ($J_{ave} \leq 100$, Ref. 15) indicating acceptable identified model accuracy and are all close to the guideline for excellent model accuracy ($J_{ave} \leq 50$, Ref. 15). Identified values for the inflow apparent mass (and static gain) parameters generally decrease in magnitude as the forward flight speed is increased. Identified values for the apparent mass coefficients approach theoretical values for Pitt-Peters dynamic inflow for the highest speed case. Identified values for the inflow apparent mass and static gain matrices are compared with Pitt-Peters theoretical values. Results are summarized in Table 4 for the hover case, where symmetry implies that “2,2” and “3,3” elements are equal. Although the identified values may differ from the Pitt-Peters theoretical values by up to an order of magnitude, the effective inflow time constant, defined as $\tau_i = L_{jj}M_{jj}$, are closer in magnitude to theory. Specifically, identified time constants for the coaxial rotor system are approximately a factor of two to three slower than Pitt-Peters dynamic inflow theory. Note that differences in the inflow time constants tend to be less significant for the overall aircraft response than the inflow static gain coefficient.

Table 4. Comparison of Identified and Theoretical Inflow Model Parameters in Hover.

Parameter	Pitt-Peters Theory	Upper Rotor	Lower Rotor
M_{11}	0.036	0.185	0.121
M_{22}	-0.0048	-0.0304	-0.0232
L_{11}	5.09	1.78	3.45
L_{22}	-20.4	-9.37	-12.9
τ_i , uniform	0.18 s	0.33 s	0.42 s
τ_i , harmonic	0.098 s	0.28 s	0.30 s

Identified values for the wake distortion coefficients decrease in magnitude as forward flight speed is increased, which is consistent with trends reported in the literature. Comparison of identified wake distortion parameters with results for an isolated rotor is provided in Table 5. Isolated rotor results are taken from Ref. 9. The tabulated results include comparison of the effective wake distortion coefficient,

$$K_{Req} = \frac{K_1 + K_2}{1 + K_M} \quad (11)$$

For an isolated rotor, the effective wake distortion coefficient is very similar to the theoretical value of 1.5 (Ref. 21). Significant reduction of the overall effect of wake distortion occurs for the coaxial rotor system. This reduction occurs primarily due to rotor-to-rotor wake interactions of the counter-rotating rotors. In general, the nature of the coaxial rotor system results in little-to-no coupling between pitch and roll motions.

Table 5. Comparison of Identified Isolated and Coaxial Rotor Wake Distortion Parameters in Hover.

Parameter	Isolated Rotor	Coaxial Rotor
K_1	0.84	0.61
K_2	2.17	0.38
K_{Req}	1.6	0.47

Linear Inflow Model Verification

Verification results for the identified second-order inflow model are shown below for the hover case. Forward flight verification results are presented later in this paper. Bare airframe response time histories are shown in Figure 3 and Figure 4, which compare the lateral and longitudinal response due to control inputs for the nonlinear simulation model with CHARM (solid lines) and the linearized inflow model (dashed lines). Very good model agreement can be seen for the short-term response. Some deviations can be observed in the low-frequency body response, indicating differences in the effective body “phugoid” mode frequency and damping.

Frequency domain comparisons of the identified model with CHARM nonlinear simulation are shown in Figure 5 and Figure 6 for the roll and pitch responses, respectively. The CHARM results were determined by applying frequency sweeps to the lateral and longitudinal controls, and transfer function estimation was performed using CIFER[®]. In addition, frequency domain comparisons include a reference model using uncoupled Pitt-Peters dynamic inflow models for each rotor. Again, it can be seen that the identified second-order inflow model captures the nonlinear CHARM simulation for frequencies greater than 1 rad/sec, which is desired for flight control development. In contrast, the Pitt-Peters reference model underpredicts the magnitude between 1-10 rad/sec of the nonlinear CHARM simulation results, which is reflected by the “model fit” cost (J_{ave}) determined using CIFER[®] cost metrics from 1 to 30 rad/sec. These differences can be attributed to the difference between the theoretical and identified inflow static gain coefficients shown in Table 4.

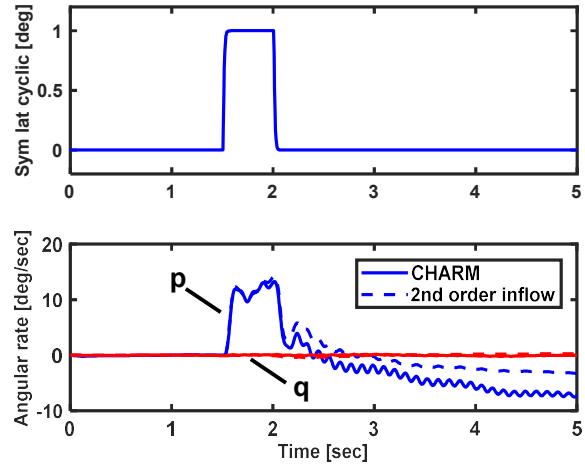


Figure 3. Identified Inflow Model Verification of GCR Bare Airframe Response for Lateral Cyclic Input in Hover.

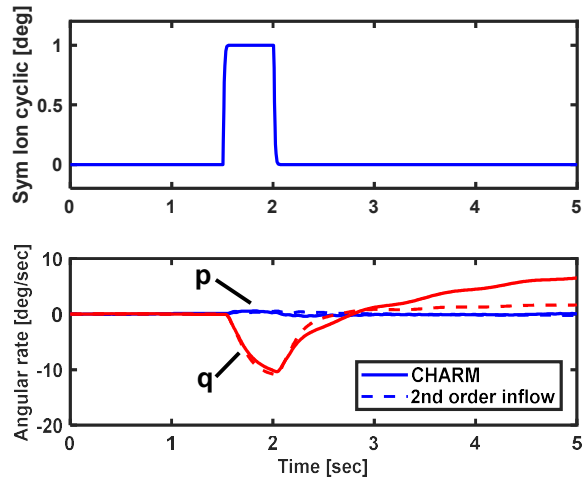


Figure 4. Identified Inflow Model Verification of GCR Bare Airframe Response for Longitudinal Cyclic Input in Hover.

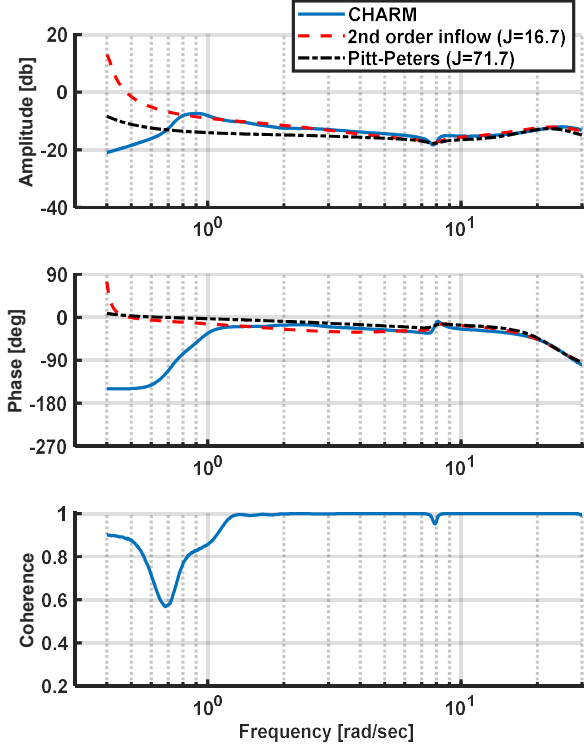


Figure 5. GCR Bare Airframe p/δ_{lat} Frequency Response Comparison.

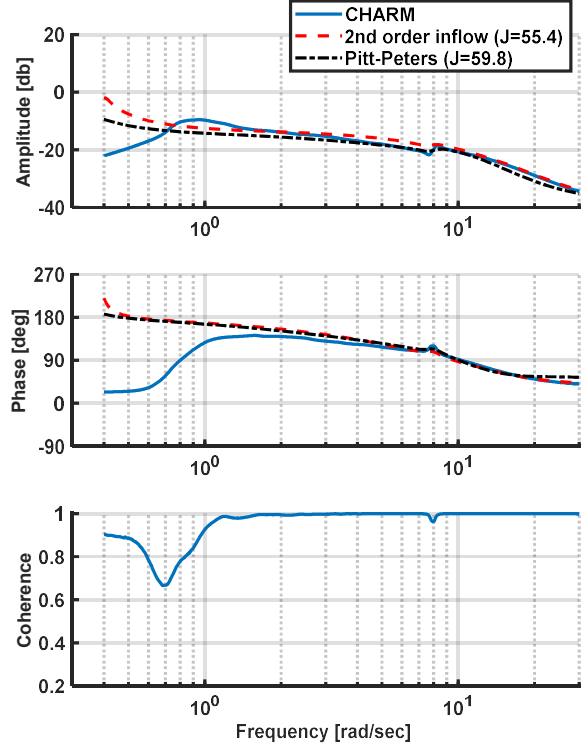


Figure 6. GCR Bare Airframe q/δ_{lon} Frequency Response Comparison.

FLIGHT CONTROLLER DESIGN STUDY

As discussed previously, one motivation for extraction of linear inflow models from higher fidelity aeromechanics analyses is to support flight control development for advanced rotorcraft configurations. It has been shown in Ref. 22 that rotor and inflow dynamics are necessary to correctly characterize stability margins in modern flight control development. The present study examines the effect of the inflow model structure in the development of a roll-axis controller for the GCR configuration in hover.

Feedback Control Architecture

The feedback controller structure is illustrated schematically in Figure 7. Aircraft sensed outputs are input to the control law, which is combined with the pilot inputs prior to the control system mixer. For this investigation, it is assumed that the primary aircraft response axes are decoupled so that each axis (roll, pitch, yaw) can be analyzed separately. Only the roll axis controller is considered in this paper. Feedback controllers for the pitch and yaw axes have been developed and implemented primarily to provide stabilization of the low frequency body modes when performing frequency sweep excitation of the nonlinear simulation model.

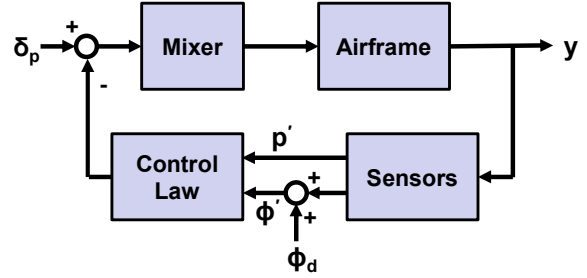


Figure 7. Flight Control System Architecture for GCR Design Study.

The roll axis controller consists of a proportional-integral-derivative (PID) structure with lagged roll rate feedback. The feedback control signal is given by the following relationship:

$$\delta_{lat_{fb}} = -K_p H_f(s) p' - \left(K_\phi + \frac{K_I}{s} \right) \phi' \quad (12)$$

where p' and ϕ' are respectively the sensed roll rate and attitude, and (K_p, K_ϕ, K_I) are controller gains. The low pass filter $H_f(s)$ on the roll rate feedback is used to attenuate the coupled rotor-body response near the regressing flap mode.

Actuator and sensor dynamics are not explicitly included with the model. An input-output delay of $\tau = 50$ msec is included in the sensor block to represent the lag associated with these dynamics.

Controller gains are determined using classical feedback control design methods (e.g., Ref. 23). Desired controller performance is assessed in terms of stability margins and crossover frequency metrics. Desired performance for gain margin, phase margin, and crossover frequency are $GM \geq 6$ dB, $PM \geq 45$ deg, and $\omega_c \approx 4$ rad/sec.

Roll Controller Design Study Results

Results of the GCR roll axis controller design study are given in this section. Controller gain selection and design metrics are determined based on a high-order linear model of the rotor-body dynamics extracted from the nonlinear flight dynamics model. Blade flap and lag degrees of freedom are retained, and the identified second-order inflow model from the previous section of this paper is coupled with the rotor-body dynamics. Results compare controller performance with the nonlinear CHARM simulation, which serves as the “truth” model for this study. In addition, comparisons are made with model predictions using uncoupled Pitt-Peters inflow models for the rotor system to assess the sensitivity of the inflow model structure.

The lightly-damped rotor-body mode around $\omega = 25$ rad/sec of the roll axis response (see Figure 5) provided difficulties when determining controller gains to satisfy the desired design specifications. Specifically, it was found that conventional lagged-rate feedback was insufficient, and a second-order filter structure was needed for $H_f(s)$ in Eq. 12. Figure 8 illustrates this behavior, where it can be seen that the second-order filter pulls the roll-regressing flap mode branch farther into the left-hand plane of the root locus plot than the first order filter.

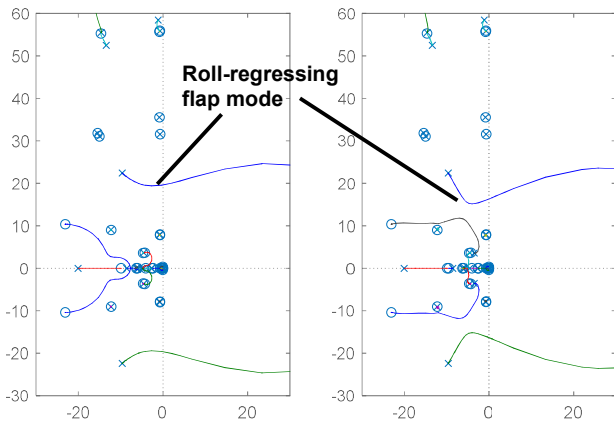


Figure 8. Roll Axis Controller Root Locus with First Order Filter (left) and Second Order Filter (right) for Roll Rate Feedback.

Using a second-order filter on roll rate with break frequency of 5 rad/sec and integral feedback time constant of 4 sec, controller gains were determined to yield a crossover frequency of 4 rad/sec. Specifically, controller rate, attitude, and integral gains were found to be:

$$\begin{aligned} K_p &= 0.046 \text{ deg/deg/sec} \\ K_\phi &= 0.23 \text{ deg/deg} \\ K_I &= 0.057 \text{ deg/deg} \end{aligned}$$

Roll controller metrics are summarized in Table 6, which include crossover frequency (ω_c), gain / phase margins (GM, PM), and disturbance rejection bandwidth / peak (DRB, DRP) as defined in Ref. 23. Values in the column labeled “CHARM” are determined by applying frequency sweep inputs to the pilot command and sensor disturbance inputs (δ_p and ϕ_d signals in Figure 7) for the nonlinear CHARM simulation. These results represent “truth” for this study. The remaining columns of Table 6 correspond to predicted performance based on the high-order linear model with identified second-order inflow and uncoupled Pitt-Peters inflow models.

The corresponding controller broken loop and disturbance rejection responses respectively are shown in Figure 9 and Figure 10 for each model case. It can be seen that the linearized second-order inflow model accurately captures the nonlinear CHARM model in the crossover region. Correspondingly, the crossover frequency ω_c , stability margins, and disturbance rejection bandwidth ($|\phi'/\phi_d|_{-3dB}$) compare favorably. The discrepancy observed for the disturbance rejection peak ($|\phi'/\phi_d|_{peak}$) occurs since the nonlinear CHARM simulation results in more excitation of the regressing lag mode at approximately 7 rad/sec in Figure 10.

Table 6. GCR Roll Controller Performance Metrics.

Metric [Units]	CHARM	Second-order inflow	Pitt-Peters inflow
ω_c [rad/sec]	4.4	4.0	3.4
GM [dB]	12.0	14.0	15.0
PM [deg]	60	53	74
DRB [rad/sec]	2.0	2.0	1.5
DRP [dB]	2.3	1.2	1.1

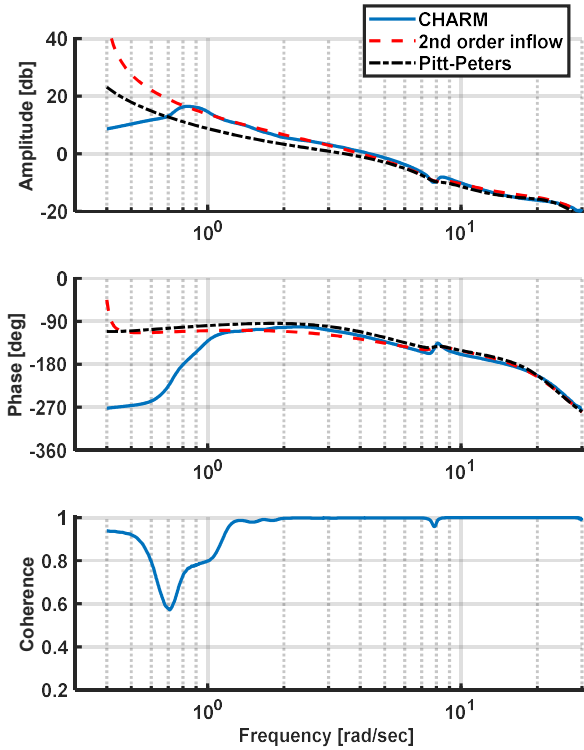


Figure 9. GCR Roll Controller Broken Loop Response $\delta_{lat_{fb}}/\delta_{lat_{mixer}}$ Comparison.

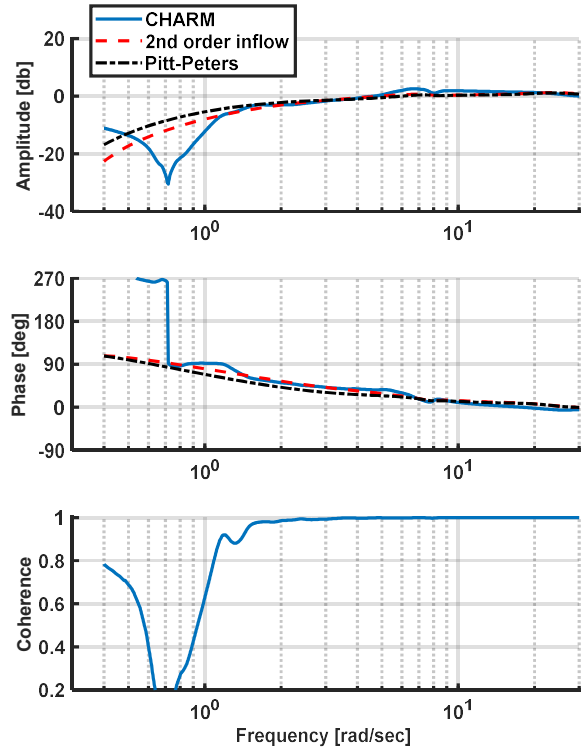


Figure 10. GCR Roll Controller Disturbance Rejection Response ϕ'/ϕ_d Comparison.

In contrast, using the uncoupled Pitt-Peters reference model to determine controller performance results in the crossover and DRB frequencies being underpredicted and would indicate a sluggish response. Furthermore, the predicted phase margin using uncoupled Pitt-Peters is over-estimated when compared to the CHARM truth model and second-order inflow model, thus giving an over-estimate of closed-loop damping and robustness to uncertainty.

One additional illustration of the effect of the inflow model on predicted controller performance is provided. Figure 11 compares the predicted closed response for both inflow models with the CHARM nonlinear response. The identified second-order inflow model can be seen to match the CHARM response well. While this case study suggests sufficient design margins can be achieved, it also underscores the importance of an accurate inflow model structure to ensure controller design performance is maintained.

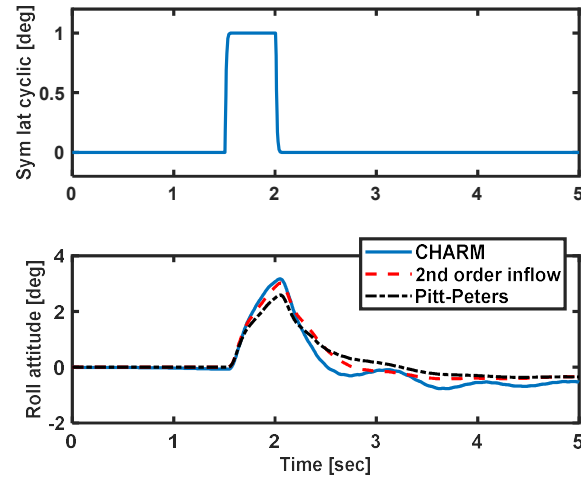


Figure 11. GCR Closed Loop Response to Symmetric Lateral Cyclic Input.

FORWARD FLIGHT MODELING CONSIDERATIONS

In addition to rotor-to-rotor interactions, interference effects between the coaxial rotor system wake and the empennage are relevant in forward flight operational conditions. These interference effects affect the trim condition and occur due to changes of the wake geometry in forward flight. Previous work (Ref. 24) has shown that interference effects can also impact the dynamic response characteristics. These dynamic response effects occur due to non-uniformities of the induced velocity field, which give rise to additional cross-coupling effects such as pitch due to sideslip and yaw due to angle of attack variations.

To include empennage interference effects in the nonlinear CHARM flight dynamics model, off-rotor evaluation points are included with the rotor blade control points when calculating the free wake induced velocity field. These flow field evaluation locations correspond to the empennage surface reference points, as well as several locations along the surface span. Multiple evaluation points per surface allow local flow field non-uniformities to be averaged to yield a more representative estimate of the surface downwash or sidewash angle perturbation. For the pusher propeller, which is represented using a rotor disk model, multiple wake induced velocity locations are distributed radially and azimuthally to capture non-uniform inflow effects. Local interference velocity components are resolved into uniform and harmonic inflow perturbations, which can be applied to the disk model aerodynamic force and moment coefficient calculation.

Forward flight trim characteristics for the GCR configuration are shown in Figure 12, which compare the CHARM simulation model with a baseline model that consists of uncoupled Pitt-Peters inflow models for each rotor and no empennage interference effects. In addition, results for the CHARM nonlinear simulation are shown with and without interference effects applied to the empennage and pusher propeller to assess the importance of these effects for this rotorcraft configuration. Note that the pusher prop collective is used as a trim control, in addition to symmetric collective and longitudinal cyclic pitch, and the trim pitch attitude is zero. Directional trim is primarily controlled by differential collective. Small but non-zero lateral cyclic and roll attitude are also needed for lateral trim of the CHARM nonlinear simulation. It can be seen that trim symmetric collective is higher with the CHARM induced velocity model. Longitudinal and directional trim characteristics also are affected by higher fidelity wake and interference effects.

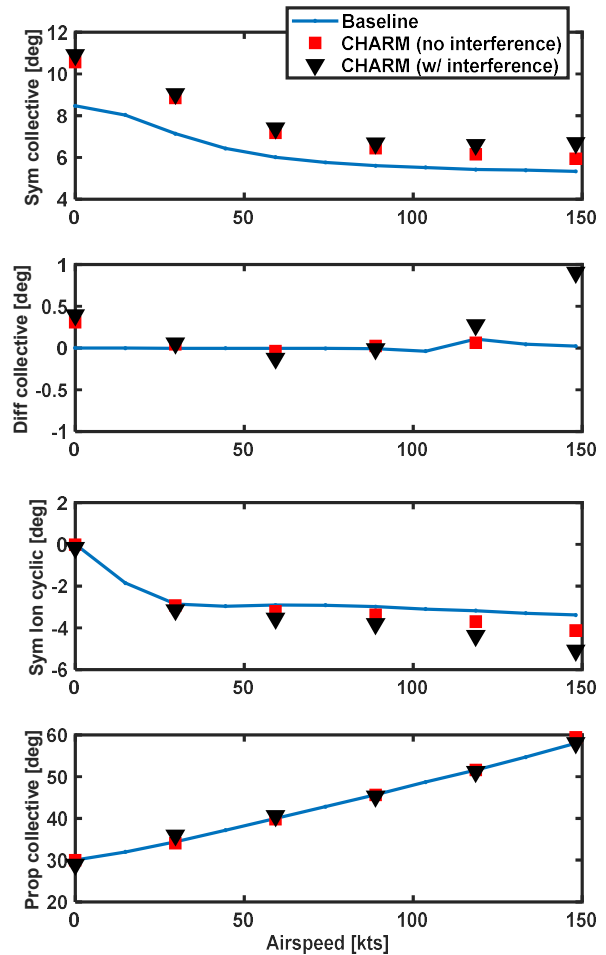


Figure 12. GCR Forward Flight Trim Characteristics.

The bare airframe response of the GCR configuration due to a longitudinal cyclic pulse input is shown in Figure 13. Comparison is made between the baseline (no interference) model with CHARM nonlinear simulation (with and without empennage interference effects). Note that the longitudinal input causes a secondary yaw response due to the pusher prop aerodynamics. While this off-axis response is similar between the baseline and CHARM models, and relatively unaffected by the coaxial rotor system interference, differences can be seen in the long-term on-axis response. Note that only small differences due to empennage interference are observed since the induced velocity field for the coaxial rotor is relatively symmetric downstream of the rotor system.

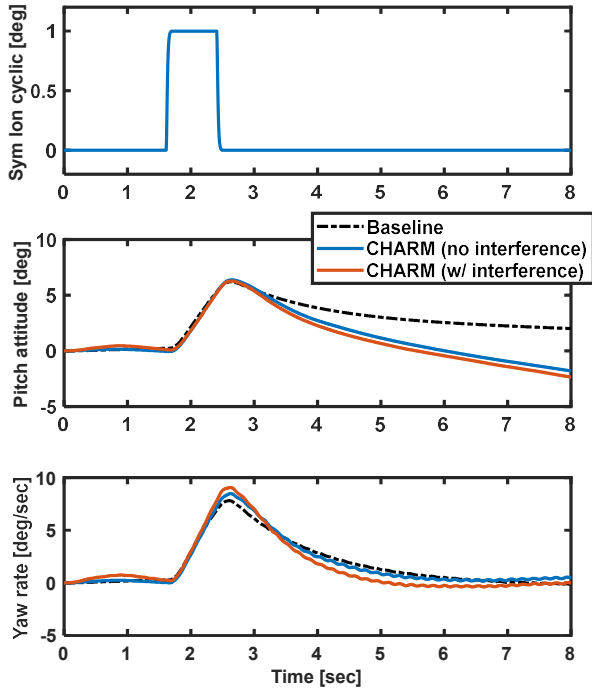


Figure 13. GCR Bare Airframe Response due to Longitudinal Input from 80-kts Level Flight Trim.

Finally, comparisons of the identified second order inflow model with CHARM nonlinear simulation are shown in Figure 14 and Figure 15. Figure 14 shows the on-axis (roll) response and off-axis responses due to a symmetric lateral cyclic input. Figure 15 illustrates the corresponding on-axis (pitch) and off-axis responses due to a symmetric longitudinal cyclic input. It can be seen that the identified inflow model captures the dynamic response behavior for the full nonlinear CHARM flight dynamics simulation, providing verification of the identified inflow model structure.

CONCLUSIONS

Extraction of linear inflow models from higher fidelity free wake analysis has been performed for a modern lift-offset coaxial rotorcraft configuration. Linear inflow models were determined for a second-order inflow model structure that includes wake distortion effects due to pitch and roll motions. The following specific conclusions can be drawn from this work:

1. Identified second-order inflow models were determined for a generic coaxial rotorcraft and were shown to accurately represent the short-term response when compared to the nonlinear flight dynamics simulation with CHARM free wake model.

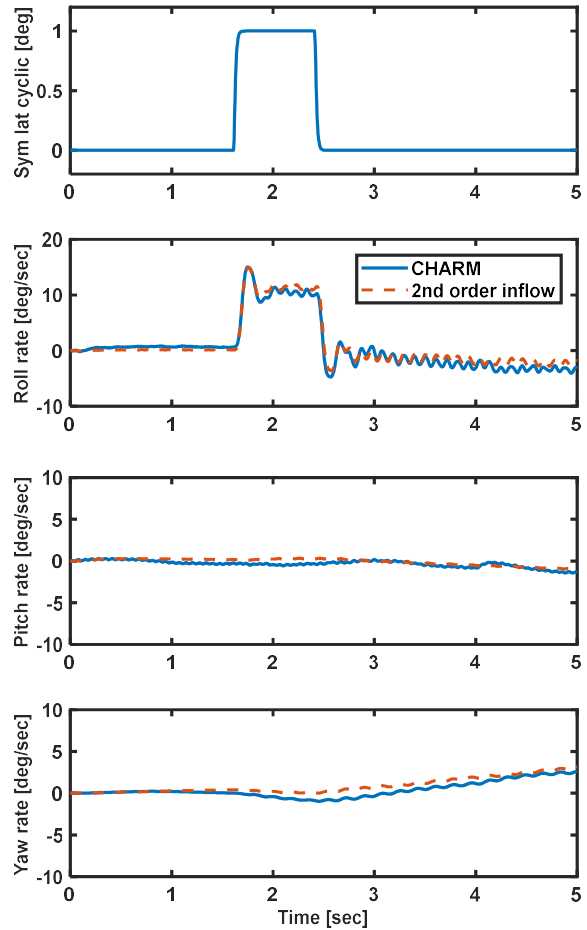


Figure 14. Identified Inflow Model Verification of GCR Bare Airframe Response for Lateral Cyclic Input in 80kt Forward Flight.

2. The static gain coefficients for the identified inflow model are significantly larger for the coaxial rotor system as compared to theoretical values determined from Pitt-Peters dynamic inflow, although inflow time constants are closer in magnitude. Inflow wake distortion effects for the coaxial rotor system are smaller than an isolated rotor system due to rotor-to-rotor wake interactions.
3. The second-order inflow model structure provides a more representative reference model for flight control development. Crossover frequency, stability margins, and disturbance rejection characteristics are more accurately predicted using the second-order linearized inflow model than a reference model based on Pitt-Peters dynamic inflow.

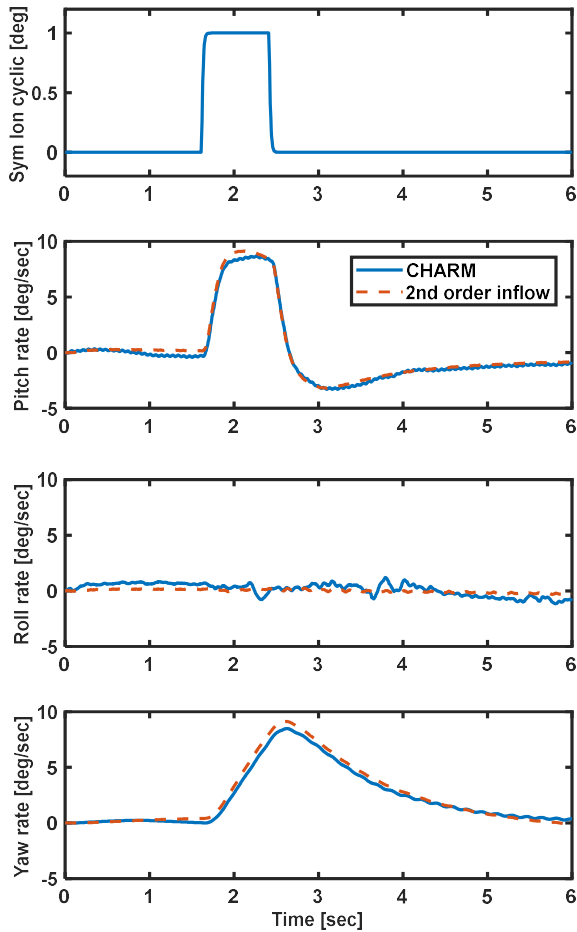


Figure 15. Identified Inflow Model Verification of GCR Bare Airframe Response for Longitudinal Cyclic Input in 80kt Forward Flight.

- The effect of the inflow/interference model on coaxial rotorcraft dynamic response characteristics is less significant in forward flight conditions.

Author contact:

Jeffrey Keller jeff@continuum-dynamics.com

Robert McKillip bob@continuum-dynamics.com

Daniel Wachspress dan@continuum-dynamics.com

ACKNOWLEDGMENTS

This work was supported by an SBIR Phase II project for the U.S. Army (Contract No. W911W6-17-C-0019), Dr. Mahendra Bhagwat and Dr. Mark Lopez serving as technical monitors.

REFERENCES

¹Pitt, D.M. and Peters, D.A., “Theoretical Prediction of Dynamic Inflow Derivatives,” *Vertica*, Vol. 5, (1), 1981, pp. 21-34.

²Peters, D.A. and He, C., “Correlation of Measured Induced Velocities with a Finite-State Wake Model,” *Journal of the American Helicopter Society*, Vol. 36, (3), July 1991, pp. 59-70.

³Juhasz, O., Xin, H., and Tischler, M.B., “Inflow Based Flight Dynamics Modeling Improvements for the Sikorsky X2 Technology™ Demonstrator,” Vertical Flight Society 76th Annual Forum and Technology Display, Virginia Beach, VA, October 2020.

⁴Rand, O., Khromov, V., Hersey, S., Celi, R., Juhasz, O., and Tischler, M., “Linear Inflow Model Extraction from High-Fidelity Aerodynamic Models for Flight Dynamics Applications,” American Helicopter Society 71st Annual Forum, Virginia Beach, VA, May 2015.

⁵Rand, O. and Khromov, V., “Free Wake Based Dynamic Inflow Model in Hover, Forward, and Maneuvering Flight,” American Helicopter Society 72nd Annual Forum, West Palm Beach, FL, May 2016.

⁶He, C. Syal, M., Tischler, M.B., and Juhasz, O., “State Space Inflow Model Identification from Viscous Vortex Particle Method for Advanced Rotorcraft Configurations,” American Helicopter Society 73rd Annual Forum, Fort Worth, TX, May 2017.

⁷Hersey, S., Celi, R., Juhasz, O., and Tischler, M.B., “Accurate State Space Inflow Modeling for Flight Dynamics and Control of a Coaxial-Pusher Rotorcraft,” AHS International 74th Annual Forum, Phoenix, AZ, May 2018.

⁸Keller, J.D., McKillip, R.M., Wachspress, D.A., Tischler, M.B., and Juhasz, O., “A Free Wake Linear Inflow Model Extraction Procedure for Rotorcraft Analysis,” American Helicopter Society 73rd Annual Forum, Fort Worth, TX, May 2017.

⁹Keller, J.D., McKillip, R.M., Jr., Wachspress, D.A., Tischler, M.B., and Juhasz, O., “Linearized Inflow and Interference Models from High Fidelity Free Wake Analysis for Modern Rotorcraft Configurations,” Vertical Flight Society 75th Annual Forum, Philadelphia, PA, May 2019.

¹⁰He, C., Gladfelter, M., Chang, C., Tischler, M.B., and Juhasz, O., “VPM Derived State Space Inflow Model for Multi-rotor Air Vehicle Modeling and Simulation,” Vertical Flight Society 75th Annual Forum, Philadelphia, PA, May 2019.

¹¹Wachspress, D.A., Keller, J.D., Quackenbush, T.R., Whitehouse, G.R., and Yu, K., “High Fidelity Rotor Aerodynamic Module for Real Time Rotorcraft Flight Simulation,” American Helicopter Society 64th Annual Forum, Montreal, Canada, April 2008.

- ¹²Spoldi, S. and Ruckel, P., “High Fidelity Helicopter Simulation using Free Wake, Lifting Line Tail, and Blade Element Tail Rotor Models,” American Helicopter Society 59th Annual Forum, Phoenix, AZ, May 2003.
- ¹³Keller, J.D., Wachspress, D.A., and Hoffler, J.C., “Real Time Free Wake and Ship Airwake Model for Rotorcraft Flight Training Application,” American Helicopter Society 71st Annual Forum, Virginia Beach, VA, May 2015.
- ¹⁴Keller, J.D., Wachspress, D.A., and Hoffler, J.C., “Pilot Evaluation of a Real Time Free Wake Model in a Navy Rotorcraft Fleet Trainer,” American Helicopter Society 73rd Annual Forum, Fort Worth, TX, May 2017.
- ¹⁵Tischler, M.B, and Remple, R.K., *Aircraft and Rotorcraft System Identification, Second Edition*, AIAA Education Series, Reston, VA, 2012.
- ¹⁶Berger, T., Juhasz, O., Lopez, M.J.S., Tischler, M.B., and Horn, J.F., “Modeling and Control of Lift Offset Coaxial and Tiltrotor Rotorcraft,” presented at the 44th European Rotorcraft Forum, Delft, The Netherlands, September 2018.
- ¹⁷Johnson, W., Moodie, A.M., and Yei, H., “Design and Performance of Lift Offset Rotorcraft for Short Haul Missions,” American Helicopter Society Future Vertical Lift Aircraft Design Conference, San Francisco, CA, January 2012.
- ¹⁸Hersey, S., Celi, R., Juhasz, O., Tischler, M.B., Rand, O., and Khromov, V., “State Space Inflow Model Identification and Flight Dynamics Coupling for an Advanced Coaxial Rotorcraft Configuration,” American Helicopter Society 73rd Annual Forum, Fort Worth, TX, May 2017.
- ¹⁹Fegely, C., Xin, H., Juhasz, O., and Tischler, M.B., “Flight Dynamics and Control Modeling with System Identification Validation of the Sikorsky X2 Technology™ Demonstrator,” American Helicopter Society 72nd Annual Forum, West Palm Beach, FL, May 2016.
- ²⁰Juhasz, O., Syal, M., Celi, R., Khromov, V., Rand, O., Ruzicka, G.C., and Strawn, R.C., “Comparison of Three Coaxial Aerodynamic Prediction Methods Including Validation with Model Test Data,” *Journal of the American Helicopter Society*, Vol. 59, (3), July 2014.
- ²¹Keller, J.D., “An Investigation of Helicopter Dynamic Coupling Using an Analytical Model,” *Journal of the American Helicopter Society*, Vol. 41, (4), October 1996, pp. 322-330.
- ²²Curtiss, H.C., Jr., “Stability and Control Modeling,” Proceedings of the 12th European Rotorcraft Forum, Garmisch-Partenkirchen, Federal Republic of Germany, September 1986.
- ²³Tischler, M.B., Berger, T., Ivler, C.M., Mansur, M.H., Cheung, K.K., and Soong, J.Y., *Practical Methods for Aircraft and Rotorcraft Flight Control Design: An Optimization-Based Approach*, AIAA Education Series, Blacksburg, VA, 2017.
- ²⁴Curtiss, H.C., Jr. and Quackenbush, T.R., “The Influence of the Rotor Wake on Rotorcraft Stability and Control,” Proceedings of the 15th European Rotorcraft Forum, Amsterdam, Netherlands, September 1989.